Author/s:
Sier, D;Ekanayake, RSK;Chantler, CT

Title:
The significance of fluorescence in transmission X-ray absorption spectroscopy and X-ray absorption fine structure

Date:
2022-01-01

Citation:
Sier, D., Ekanayake, R. S. K. & Chantler, C. T. (2022). The significance of fluorescence in transmission X-ray absorption spectroscopy and X-ray absorption fine structure. X Ray Spectrometry, 51 (1), pp.91-100. https://doi.org/10.1002/xrs.3262.

Persistent Link:
https://hdl.handle.net/11343/298881

The Significance of Fluorescence in Transmission X-ray Absorption Spectroscopy and X-ray Absorption Fine Structure

Daniel Sier

E-mail: dsier@student.unimelb.edu.au

Ruwini S K Ekanayake

E-mail: rekanayake@student.unimelb.edu.au

C T Chantler*

E-mail: chantler@unimelb.edu.au
School of Physics, The University of Melbourne, Melbourne Australia

Abstract. We present a method to explore the effect of fluorescence on X-ray attenuation measurements obtained from X-ray absorption spectroscopy (XAS). We use the X-ray extended range technique-like method (XERT-like). The experimental setup includes different sized apertures to control the number of secondary X-rays entering the detector. Comparison of attenuation measurements produced with different aperture combination permit investigation of the effect of fluorescence radiation. In this work, fluorescence has a large impact upon the attenuation measurements of thick zinc foils. The correction is energy-dependent and sample thickness-dependent and changes the structure and relative amplitudes of oscillations in the near-edge region. Correction for this systematic is important for absolute measurement, for edge-jump and edge characterisation, and for near-edge structure and amplitudes. A significant background scattering due to zinc fluorescence from the beamline optics was identified and treated for the first time. The model theory fits the experimental measurements well. The resulting correction is most significant for thicker foils with the 50 μm sample experiencing a shift in attenuation of up to 15.5% for the largest aperture while the 25 μm and 10 μm samples saw corrections of up to 0.153% and 0.00639% respectively. The standard error from the dispersion and variance was reduced by up to 50.5% after the correction for the 50 μm sample. This enables high-accuracy data and theoretical and experimental analysis to below 0.03% accuracy. The technology is advanced. There is a cost in preparation and measurement time of less than a factor of two, and the principles are clear and can be routinely implemented on any beamline. This paper focuses on the model and parameters for fluorescence.

keywords: Transmission X-ray Absorption spectroscopy; Fluorescence Radiation; X-ray Absorption Fine Structure

1. Introduction

X-ray absorption fine structure (XAFS) is one of the best techniques for investigating chemical states and local environments of condensed or disordered materials, in the fields of biology, environmental science, crystallography, material science and medical sciences [1, 2, 3, 4, 5, 6, 7]. However, widely used XAFS techniques are limited by experimental uncertainty and unevaluated systematic effects. In XAFS analysis, treating systematic effects and obtaining experimental uncertainties are crucial for deeper insight across all fields [8, 9, 10].

The effect of fluorescence due to secondary photons has a considerable impact on the measured (transmission) mass attenuation coefficients of materials in X-ray physics. Secondary photons are produced when the X-ray beam is absorbed and reemitted from the sample material at an angles or by air path of the X-ray beam. When X-rays interact with a material, they are scattered elastically (coherent scattering and often labelled Rayleigh scattering for isolated scatterers) and inelastically (often labelled incoherent scattering and often dominated by Compton scattering) while X-ray fluorescence (often labelled resonant inelastic X-ray RIX[S] or resonant X-ray emission RXE[S]) is also produced in the absorbing material [11]. X-ray fluorescence is significant at and above the absorption energy, whereas the effects of Laue-Bragg scattering and thermal diffuse scattering are significant at specific energies, and Rayleigh scattering is generally a smooth function. Smooth inelastic scattering (Non-resonant) is observed below and above the absorption edge in the form of Compton, plasmonic and optical molecular interactions [12, 13] and is dipolar in nature to first order and hence primarily directed through a scattering angle of $\pi/2$; hence the impact on a transmission measurement as in this experiment serves primarily to reduce the transmitted intensity of the beam and becomes significant and dominant for high[er] energy X-ray regions. X-ray optics, photon energy, detector response function, collimation and thickness of the material are key parameters in calculating the magnitude and significance of fluorescence in an attenuation measurement. To determine the mass attenuation coefficient $\left[\frac{\mu}{\rho}\right]_{tot}$ or $\left[\frac{\mu}{\rho}\right]$ or the linear attenuation coefficient, one must include the fluorescent photons entering both the upstream and downstream detectors. The fluorescence contributions need to be extracted when deriving the photoelectric component of the mass attenuation coefficient, the mass absorption coefficient $\left[\frac{\mu}{\rho}\right]_{pe}$ or the linear absorption coefficient, and any cross-sections or form factor data (Eqn 1) [14, 15, 16, 13]. The magnitude of XAFS oscillations are affected by the fluorescence contribution.

$$\begin{aligned} \left[\frac{\mu}{\rho}\right]_{tot} &= \left[\frac{\mu}{\rho}\right]_{pe} + \left[\frac{\mu}{\rho}\right]_{C} + \left[\frac{\mu}{\rho}\right]_{R} \\ \left[\frac{\mu}{\rho}\right]_{observed} &= \left[\frac{\mu}{\rho}\right] - \Delta\left[\frac{\mu}{\rho}\right]_{F} \end{aligned} \tag{1}$$

Here, *pe* denotes the photoelectric contribution, C denotes Compton scattering, R denotes the Rayleigh scattering, F denotes the fluorescent radiation and Δ represents the

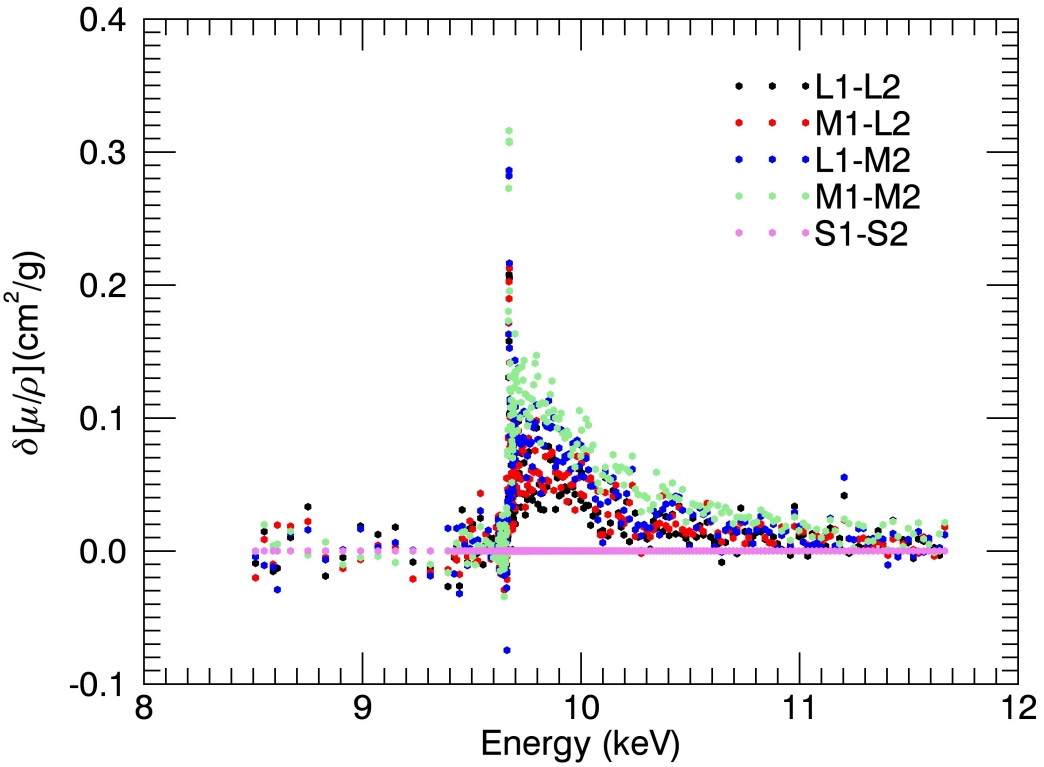

Figure 1. Discrepancy between the mass attenuation coefficient measured with the different apertures and the smallest reference aperture for 25 μm foil. Fluorescence is significant above the absorption edge. The discrepancy reaches 0.1% immediately above the absorption edge. Fluorescence below the edge is insignificant. The measured attenuation of the X-ray beam through the sample material is mainly affected, in a structure-dependent manner, by the fluorescence rather than by Rayleigh or non-resonant inelastic scattering. S1-S2, M1-M2, M1-L2, L1-M2, L1-L2 represent the different aperture combinations (small$_{up}$-small$_{down}$, medium$_{up}$-medium$_{down}$, medium$_{up}$-large$_{down}$, large$_{up}$-medium$_{down}$ and large$_{up}$-large$_{down}$).

contribution from the extra fluorescence radiation reaching upstream and downstream detectors.

Installing apertures, collimators, absorbing material, Compton scattering slits, Soller slits and diffracting crystals have been explored to exclude secondary photons from the intensity counters of the ion chambers [17, 18, 8, 19, 20, 21]. These can be effective at minimizing scattering and fluorescence contributions but do not allow accurate quantification of the contributions. However, the fluorescence can be measured precisely by varying the solid angular acceptance of the detectors and hence varying the fluorescence entering the detectors.

The X-ray Extended Range Technique (XERT) experimental setup has two daisy wheels each with different sizes of apertures to control the number of secondary X-rays

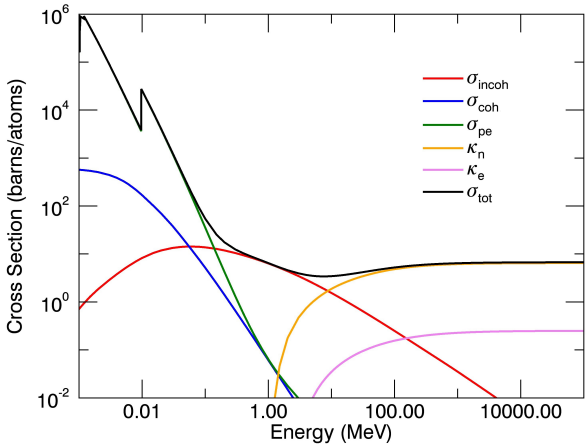

Figure 2. Cross-sections for zinc atoms of photoabsorption: $\tau = \sigma_{pe}$, coherent Rayleigh scattering-σ_{coh}, incoherent (Compton) scattering-σ_{incoh}, nuclear-field pair production-κ_n, and electron-field pair (triplet) production-κ_e contributions to the total cross section-σ_{TOT} over the energy range from 1 keV to 100 GeV.

entering the detector. This technique had been used to observe and measure scattering and fluorescence [20, 13, 22, 2, 23]. Inelastic (Compton) and elastic (Rayleigh) scattered photons and fluorescence radiation have different angular dependencies in the forward and backward directions, but both remove X-ray intensity from the primary beam and hence add to the attenuation.

Here, XERT was used to collect XAFS of zinc metal foils [24, 25]. The major source of secondary X-rays was fluorescent radiation (Fig. 1). Cross-sections for Rayleigh (i.e. coherent but isolated elastic) and Compton (i.e. non-resonant inelastic) scattering vary slowly and smoothly with energy (Fig. 1)[26, 13]. If the measurements obtained in this experiment were significantly affected by Rayleigh or Compton scattering, then the effect would be observed below and above the K edge. Other processes such as pair production, triplet production and photonuclear absorption are negligible below energies of $E \simeq 1$ MeV [27, 28, 26].

2. Effect of Fluorescence Radiation

When X-rays are absorbed, an electron may be excited to a higher energy level, creating a vacancy in a lower level at the absorption energy. Then the excited electron can relax to fill the vacancy releasing a photon, fluorescence radiation, with characteristic energies given by the bound-bound transitions. Bound electrons can alternatively be ejected when relaxing an excited electron to the lower level known as Auger or Coster-Kronig processes [29]. The signature of fluorescence radiation can be detected from the incident and transmitted ion chamber readings as an apparent shift in the mass attenuation coefficients.

Dominant characteristic fluorescent radiation arises from electron transitions from $2p_{3/2}$ to $1s$, $K\alpha_1$, from $2p_{1/2}$ to $1s$, $K\alpha_2$ and from $3p$ to $1s$, K_β. In this experiment, zinc metal produced $K\alpha_1$, $K\alpha_2$ and $K\beta$ fluorescence X-rays with energies of 8.639 keV, 8.616 keV and 9.573 keV [30, 31].

The fluorescence yield ω_i, the probability of the emission of a fluorescence photon from the process of filling a vacancy in an orbital, is a common parameter used to quantify the relative probability of fluorescence:

$$\omega_i = \frac{\Gamma_i}{\Gamma_{tot}} \tag{2}$$

where i is the orbital or sub-shell (K-shell, L-shell, M-shell...). Γ_i is the partial line width due to fluorescence and Γ_{tot} is the total line width due to fluorescence, Auger and Coster-Kronig processes [13]. The sum of the radiative yield (fluorescence yield) ω, radiationless (Coster-Kronig) yield f and Auger yield a is unity [32, 33].

$$\omega + f + a = 1 \tag{3}$$

Usually, fluorescence photons produced from other outer shells are much less significant. K-shell fluorescence is a function of the absorption coefficient and sample thickness, affected by detector noise, efficiency, experimental geometry, self-absorption, sample impurity and x-ray transport.

3. Model of Fluorescence

We assume: 1. that $K\alpha_1$ is the dominant fluorescence; and 2. that the detector efficiency for the fluorescent photons is the same as the detector efficiency for the beam photons (it may differ by factor of two or more). Aperture dependent scattering of the sample, and background window scattering, were the main contributions of the fluorescence model to the attenuation; fluorescence yield and K-shell attenuation were also incorporated. The absolute values of the area of the apertures and distances were known and implemented in the fluorescence model. A scale normalised correction for the detector efficiency and the fluorescence yield of the spectrum and $K\alpha_2$ but was consistent with unity (i.e. no additional physics). The fluorescence model considers the K-shell holes in the absorber, attenuation of the fluorescence photons in the foil and the probability of the photon entering the detectors.

Consider a sample foil of thickness t. X-rays are incident on the sample foil and hence the fluorescence photons are produced at a depth x through the sample. The number of K-shell fluorescence photons produced by the incident X-rays in the sample

is given by differential Beer-Lambert equation:

$$\begin{aligned} \frac{dI_f}{dx} &= \left[\frac{\mu}{\rho}\right]_K \rho I_x \\ I_x &= I_0 e^{\left\{-\left[\frac{\mu}{\rho}\right]_S [\rho x]\right\}} \\ \Rightarrow \frac{dI_x}{dx} &= \left[\frac{\mu}{\rho}\right]_K \rho I_0 e^{\left\{-\left[\frac{\mu}{\rho}\right] [\rho x]\right\}} \end{aligned} \tag{4}$$

where I_x is the number of photons produced at depth x through the foil, I_f is the fluorescence photon flux produced by K-shells, $\left[\frac{\mu}{\rho}\right]_K$ is the mass absorption coefficient for photoionization of the K-shell electron, $\left[\frac{\mu}{\rho}\right]_S$ is the mass absorption coefficient of the sample, I_0 is the incident photon flux and ρ is the density of the sample.

It is well known that complex processes occur near the edge, including multiple scattering XANES and XAFS oscillations, and also in principle including many-body onsets and evolution as seen in complex resonant X-ray emission spectroscopy (RXES) or resonant inelastic X-ray scattering (RIXS). Rather than assume the nature of these, the purpose of this experiment is to measure any structure experimentally. Thus $\left[\frac{\mu}{\rho}\right]_K$ (the mass absorption coefficient for the K-shell) was in this analysis obtained by subtracting all other attenuation processes including photoelectric absorption from higher shells, Rayleigh and Compton scattering, which are much more well defined theoretically and minor at these energies, from the 10 μm attenuation measurements. These processes are smooth and slowly-varying. Of course the model and theory can be used in a variety of possible experimental configurations; herein it is used to extract the normal integrated XAFS signal rather than attempting to probe the complexities of the RIXS processes [34, 35]. Hence any RIXS or many-body structure will be seen in the results and indeed will be common to all sample thicknesses (so long as the samples represent the bulk properties rather than e.g. a nanosample).

Fluorescence photons at the source are isotropic. Apertures were placed just after the upstream ion-chamber and just before the downstream ion-chamber. The probability of photons reaching the ion chambers is dependent only on the solid angle Θ due to the geometrical symmetry of the experimental setup:

$$\Theta = \frac{A}{4\pi R^2} \tag{5}$$

where A is the area of the aperture and R is the distance from the sample to the aperture. Any fluorescence produced is subject to self-absorption. Therefore, the fluorescence reaching the upstream ion chamber is:

$$I_{f,up} = \int_0^t \Theta \omega_K e^{\left\{-\left[\frac{\mu}{\rho}\right]_F [\rho x]\right\}} dI_x \tag{6}$$

All apertures are narrow and the sample foils and apertures are perpendicular to the incident X-ray beam so $cos\theta \approx 1$. ω_K is the fluorescence yield, $\left[\frac{\mu}{\rho}\right]_F$ is the mass

attenuation coefficient at the fluorescence energy. Eqn 6 becomes:

$$\begin{aligned} I_{f,up} &= \Theta\omega_K \int_0^t e^{\left\{-\left[\frac{\mu}{\rho}\right]_F[\rho x]\right\}} \left[\frac{\mu}{\rho}\right]_K \rho I_0 e^{\left\{-\left[\frac{\mu}{\rho}\right]_S[\rho x]\right\}} dx \\ I_{f,up} &= \Theta\omega_K \left[\frac{\mu}{\rho}\right]_K \rho I_0 \int_0^t e^{\left\{-\left[\frac{\mu}{\rho}\right]_F[\rho x]\right\}} e^{\left\{-\left[\frac{\mu}{\rho}\right]_S[\rho x]\right\}} dx \\ I_{f,up} &= I_0 \Theta\omega_K \frac{\left[\frac{\mu}{\rho}\right]_K}{\left[\frac{\mu}{\rho}\right]_F + \left[\frac{\mu}{\rho}\right]_S} \left(1 - e^{\left\{-\left(\left[\frac{\mu}{\rho}\right]_S + \left[\frac{\mu}{\rho}\right]_F\right)[\rho t]\right\}}\right) \end{aligned} \tag{7}$$

Similarly, the number of fluorescent photons reaching the downstream ion chamber is:

$$\begin{aligned} I_{f,dwn} &= \int_0^t \Theta\omega_K e^{\left\{-\left[\frac{\mu}{\rho}\right]_F[\rho(x-t)]\right\}} dI_x \\ I_{f,dwn} &= \Theta\omega_K \left[\frac{\mu}{\rho}\right]_K \rho I_0 \int_0^t e^{\left\{-\left[\frac{\mu}{\rho}\right]_F[\rho(x-t)]\right\}} e^{\left\{-\left[\frac{\mu}{\rho}\right]_S[\rho x]\right\}} dx \\ I_{f,dwn} &= I_0 \Theta\omega_K \frac{\left[\frac{\mu}{\rho}\right]_K}{\left[\frac{\mu}{\rho}\right]_S - \left[\frac{\mu}{\rho}\right]_F} \left(e^{\left\{-\left[\frac{\mu}{\rho}\right]_F[\rho t]\right\}} - e^{\left\{-\left[\frac{\mu}{\rho}\right]_S[\rho t]\right\}}\right) \end{aligned} \tag{8}$$

The upstream and downstream Eqns (7, 8) were derived for the transmission geometry of the XERT experimental setup. Equations for a more general geometry are discussed elsewhere [36, 37]. A more detailed form for fluorescence scattering and self-absorption is given by Trevorah *et al.* [38].

4. Background Scattering

The upstream and downstream ion chamber counts with the sample removed - the blank measurements - were obtained to normalize the attenuation measurements. Electronic noise, electronic amplification and attenuation due to air path and window attenuation can be normalized using blank measurements. In this experiment, the blank measurements were measured with the different aperture combinations used with the samples, during the experiment, to explore any background scattering effects.

Fig. 3 represents a discrepancy of the blank measurements obtained with different sized aperture combinations. The plot shows a sharp peak at the edge energy 9.66 keV of zinc. Hence, we clearly observe fluorescent photons due to upstream background sources. Fig. 3 shows that this background scattering is only dependent on the downstream ion chamber configuration which implies that fluorescence arises from zinc scattering somewhere in the beam-path upstream of the upstream daisy wheel. The main X-ray beam attenuation through the thin foil is affected by the background fluorescence counts. Therefore, including background scattering in the determination of the fluorescence radiation contribution is important. This is the first model to correct for fluorescence radiation from upstream background sources.

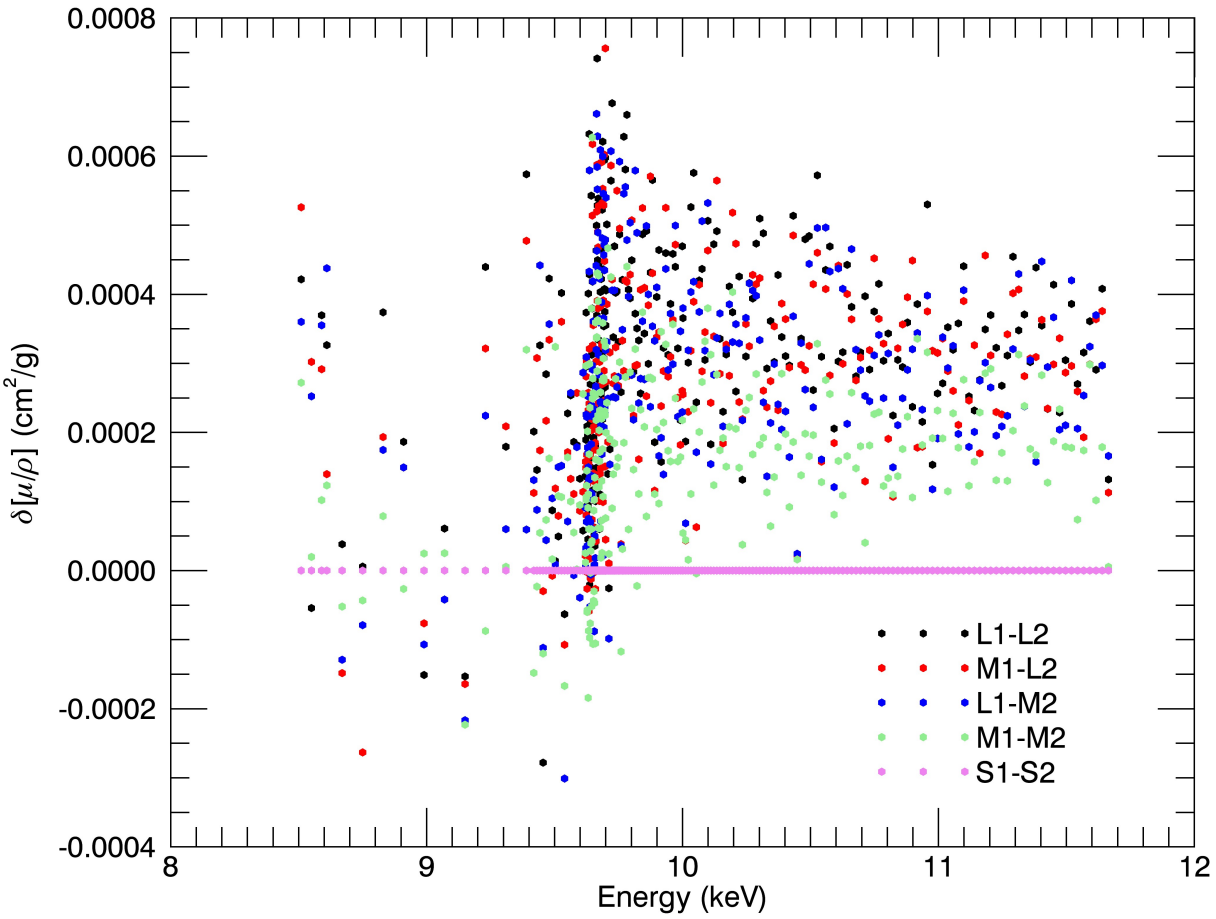

Figure 3. The discrepancy of the blank measurements obtained with different aperture combinations. S1-S2, M1-M2, M1-L2, L1-M2, L1-L2 represent the different aperture combinations discussed below (small$_{up}$-small$_{down}$, medium$_{up}$-medium$_{down}$, medium$_{up}$-large$_{down}$, large$_{up}$-medium$_{down}$ and large$_{up}$-large$_{down}$). This plot shows a zinc K edge even without a zinc sample in the beam. This background signal is fluorescent radiation produced from a background upstream zinc-containing material.

The background scattering was modelled assuming that the fluorescence radiation was coming from an unknown location upstream of the first ion chamber (R_{bg}), the location of which was determined via fitting routine

$$I_{bg,up} = I_0' \Theta(R_{bg} - R_{AP}) \frac{\left[\frac{\mu}{\rho}\right]_K}{\left[\frac{\mu}{\rho}\right]_S + \left[\frac{\mu}{\rho}\right]_F} \tag{9}$$

where $\left[\frac{\mu}{\rho}\right]_K$ is the absorption for photo-ionization of the K-shell electron, I_0' is the incident beam intensity on the fluorescent material (also determined via fitting

procedure), $\Theta(R) = A/(4\pi R)$, A is the area of the upstream ion chamber window (2.89 cm^2), R_{bg} is the distance from the source of fluorescence to the upstream ion chamber, and R_{AP} is the length of the air path between the two ion chambers. When the sample is present, the downstream ion chamber readings are also affected by the attenuation of the foil:

$$I_{bg,up} = I_0' \Theta(R_{bg}) \frac{\left[\frac{\mu}{\rho}\right]_K}{\left[\frac{\mu}{\rho}\right]_S + \left[\frac{\mu}{\rho}\right]_F} e^{\left\{-\left[\frac{\mu}{\rho}\right]_F [\rho t]\right\}} \tag{10}$$

where $\left[\frac{\mu}{\rho}\right]_F$ is the mass attenuation coefficient at the fluorescence energy.

5. Experimental

This experiment was performed at the Australian Synchrotron, where the X-ray beam was produced by a 1.9T wiggler and monochromatized by a double reflection silicon(111) crystal monochromator to a resolution of $\Delta E/E \simeq 1.5 \times 10^{-4}$. The X-ray beam was focused using Rh coated focusing mirror. Harmonic content was better than 1 part in 10^5 within the selected energy range. Beam was collimated to a 0.25×0.25 mm^2 cross section and provided photons at the sample in a rate of 10^{10} to 10^{12} γ/s. Two orthogonal slits were used to adjust the beam cross-section of 2.4 mm in horizontal and 0.4 mm in vertical directions. The incident intensities were detected by the 280 mm (active length), 310 mm (full length) long upstream ion chamber and transmitted intensities were detected by two 140 mm (active length), 170 mm (full length) long downstream ion chambers. Electronic settings of ion chambers were optimized and a continuous flow of the nitrogen was maintained for maximum stabilization of counting statistics.

The energy range of this experiment was from 8.5 keV to 11.59 keV including the K-shell absorption edge of zinc at 9.66 keV [39], covering a total of 496 energy steps. Energy calibration was achieved by accumulation of zinc, copper and tantalum transmission spectra. A finer energy grid was used at the edge and after the edge where the region that displayed fine structure. Four light tight zinc foils from Goodfellow were used in the experiment. Approximately, cross section of 25×25 mm^2, thickness ranging from 10 μm to 100 μm of zinc foils were used. Net weight of a foil is less than 1g. The purity of these foils was reported as 99.95%. These foils had Cd, Cu, In, Fe impurities of around 20 ppm each, Pb impurities of around 100 ppm and Ca, Mg, Na, Ni, Si, Sn impurities less than 10 ppm.

The sample was placed in the middle of the experimental set up (Fig. 4). Two daisy wheels with three different sized apertures along the perimeter were placed R=620 cm before and after the sample. The effective area of the small-S1, medium-M1 and large-L1 apertures were approximately $A_{S,up} = \pi(5e^{-3}/2)^2 \simeq 19.63$ mm^2, $A_{M,up} = (7e^{-3})(19e^{-3})(m^2) \simeq 133$ mm^2 and $A_{L,up} = (7e^{-3})(30e^{-3}) \simeq 210$ mm^2. Distances from the sample to either aperture were 0.620 m. Resulting solid angles Θ of the small-S1, medium-M1 and large-L1 apertures were 4.065×10^{-6}, 2.24×10^{-5} and

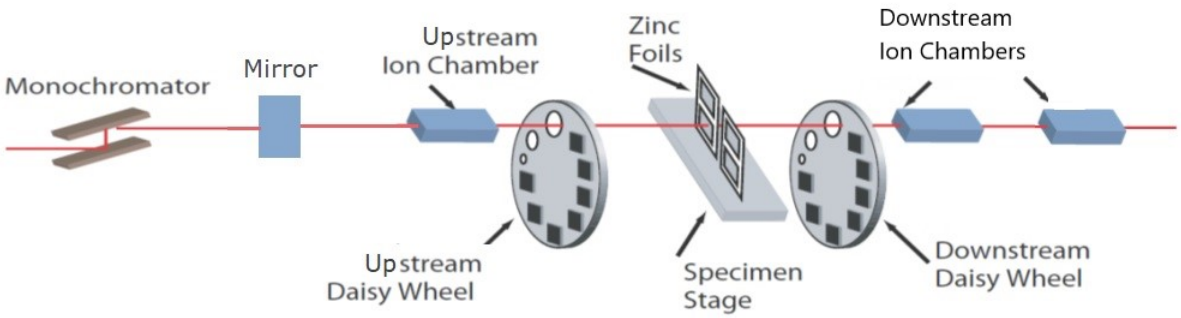

Figure 4. XERT experimental setup with two daisy wheels. Samples are placed in the middle of the experimental setup and daisy wheels are placed after the upstream ion chamber and before the downstream ion chambers. Three apertures are cut along the perimeter of daisy wheels to capture the different amount of scattering and fluorescence radiation contribution to the main beam.

4.35×10^{-5}. The effect of scattering and fluorescence was measured at each energy point using five different aperture combinations (S1-S2, M1-M2, M1-L2, L1-M2 and L1-L2).

Fig. 5 shows the variations of the fluorescence signature with the thickness of the foil. The 50 μm thick sample foil measurements are strongly affected by fluorescence while the thin 10 μm foil is less affected: 0.097% and 5.6% contributions can be observed near the absorption edge for 10 μm and 50 μm sample foils, respectively.

6. Analysis, Results and Discussion

Models of the fluorescence radiation and background scattering were fitted to the experimental fluorescence signatures. When implementing the main and background function in the fitting process, the intensity of the ion chamber can be given as:

$$I_m = I + I_f + I_{bg} \tag{11}$$

where I_m is the ion-chamber intensity for the upstream or the downstream ion-chamber, I_f is the fluorescence of the beam from the sample and I_{bg} is the background scattering and is determined via fitting routine. I is the absolute intensity of the primary beam at the ion chamber.

6.1. Fitting

The upstream and downstream intensity counts were modelled using Eqn 11 for calculating the mass attenuation coefficients obtained with all the aperture

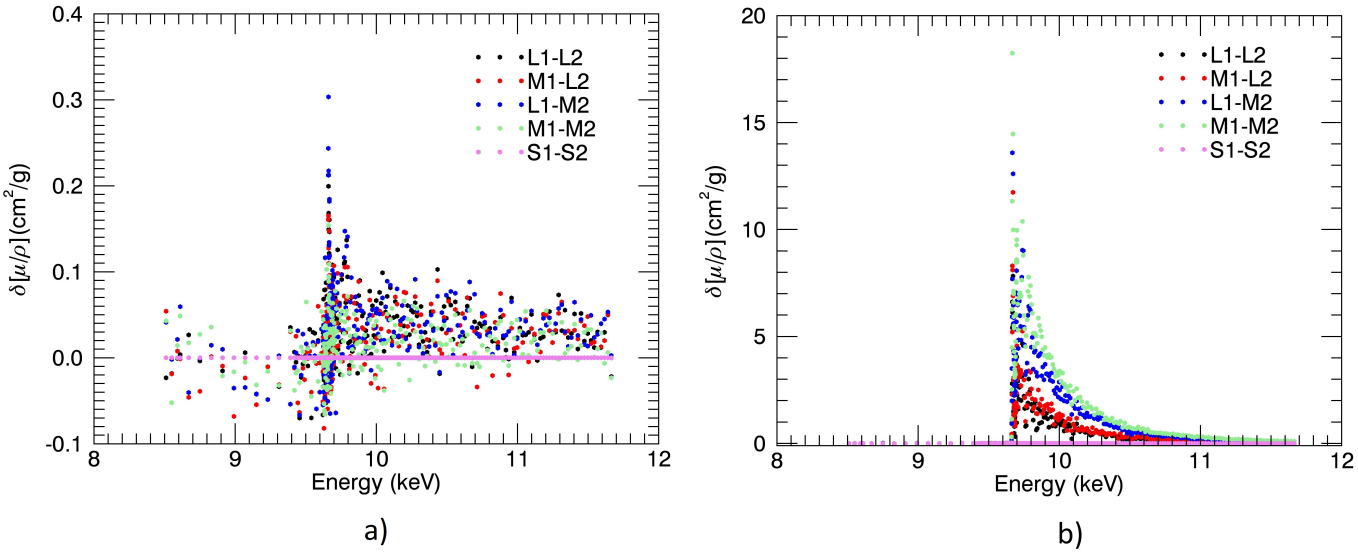

Figure 5. Discrepancies of the mass attenuation coefficients measured with different aperture combinations compared with the smallest aperture combination for: a) the 10 μm sample foil; and b) the 50 μm sample foil. Fluorescence is far more prominent with the thick sample foil. The discrepancy reaches about 0.097% and 5.6% immediately above the absorption edge for 10 μm and 50 μm sample foils respectively.

combinations. Fluorescence radiation through the sample and the background scattering terms were calculated using Eqs 7,8,9,10. The fluorescence yield for zinc metal at K-shell energy is given as 0.48 [40] and the National Institute of Standard and Technology (NIST) recommended theoretical tabulations of attenuation coefficients were used [41, 15]. Thus, the difference of the mass attenuation coefficients made with different aperture combinations and the smallest aperture combination was obtained for 10, 25 and 50 μm thick foils. Fluorescence signatures obtained from the modelled function was compared with the experimentally calculated discrepancies of mass attenuation coefficients.

Attenuation measurements of 10 μm, 25 μm and 50 μm zinc foils, together with the blank, were simultaneously fitted. The fluorescence radiation depends on the experimental geometry. In previous XERT experiments, fluorescence was investigated using simpler models [42, 13, 23]. The agreement between the model and the experimental data is strong with $\chi^2_r = 3.86$. This increases to $\chi^2_r = 4.48$ when the background scattering contribution is removed, validating the advantage of fitting all three foil and blank measurements simultaneously as well as the inclusion of the I_{bg} term.

Experimental data measured with uncertainties of the mass attenuation coefficients calculated from the point-wise variance of ten repetitions at each energy and the thickness measurement. An energy uncertainty of about 2 eV was also included in the uncertainties, important near the edge where the function has a steep slope and oscillations. This was approximately the energy step size near the edge. Best fit values of

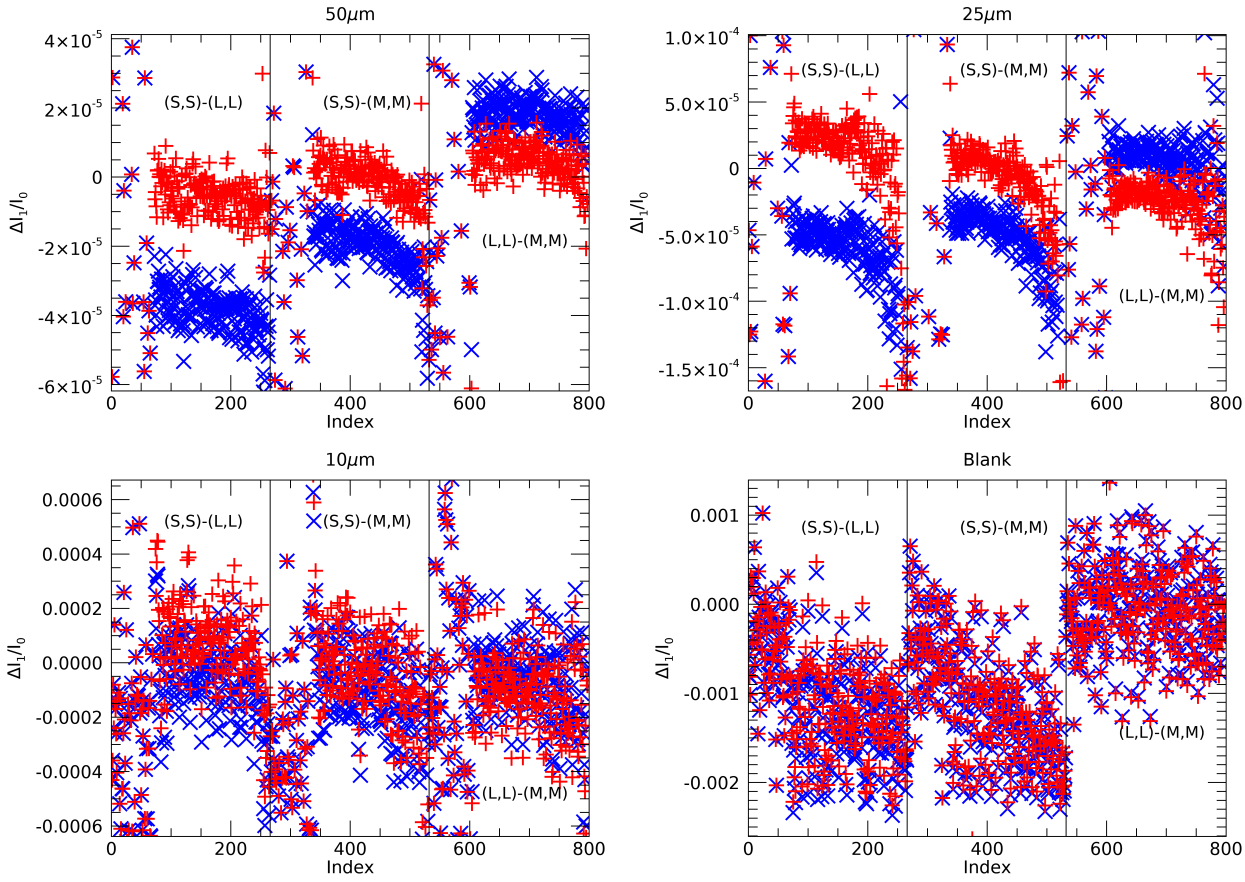

Figure 6. The raw (×) and corrected (+) data for each sample. Each set of 255 points represents one comparison of two daisy wheel aperture combinations.

the shifts were determined using a nonlinear Levenberg-Marquardt least-squares fitting routine. The best fit value of the distance of the source of background scattering from the upstream ion chamber was $4.05m$ which is roughly the position of the upstream Hutch B cryostat location.

Fig. 6 plots the difference in ion chamber ratios measured with different apertures minus that of the smallest aperture in both the raw and corrected form for all data sets. The model describes the effect of fluorescence radiation in this XERT-like experiment extremely well and illustrates an improvement over previous fluorescence analyses. Dominant contributions to χ^2_r arose from the thicker foil where the downstream flux is becoming small so that the impact of fluorescence or any scattering is becoming large; and from the larger aperture combinations where more fluorescence reaches the detector.

6.2. Correction for the effect of fluorescence.

Once the main fluorescence and background contributions are evaluated, the photon intensities of the intensity counts of the upstream and downstream ion chambers are

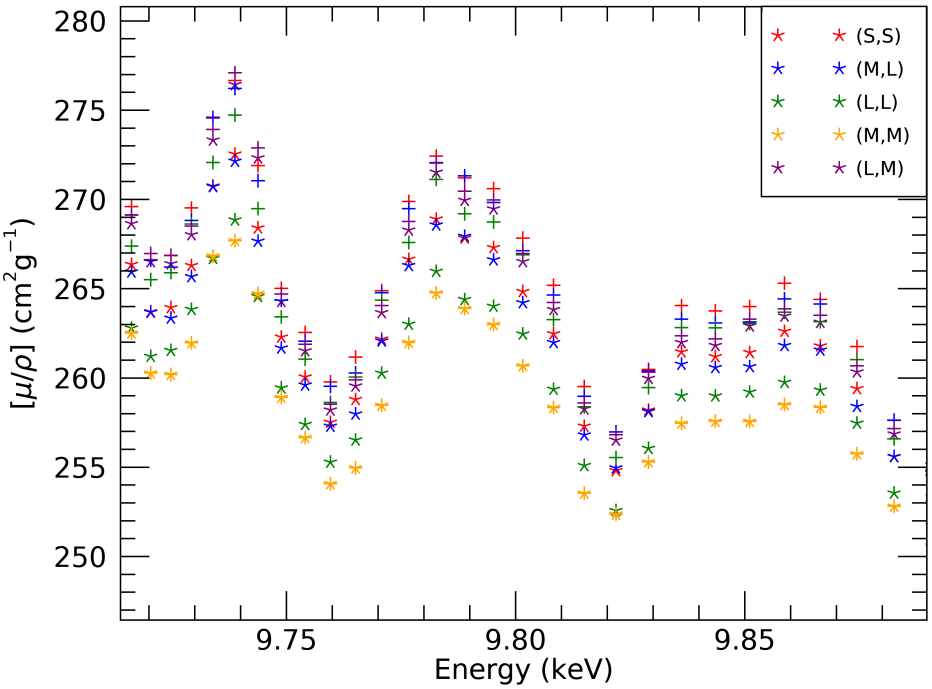

Figure 7. Discrepancy of the mass attenuation coefficients before (*) and after (+) correction for fluorescence for the 50 μm thick sample foil. The fluorescence correction minimises the discrepancy of the mass attenuation coefficient made with different aperture combinations.

corrected for the fluorescence parameters obtained:

$$I_c = I_{obs} - (I_f + I_{bg}) \tag{12}$$

where I_c is the fluorescence-corrected ion chamber counts, I_{obs} is the observed intensity counts of the ion-chambers, I_f is the main fluorescence contribution and I_{bg} is the fluorescence contribution from background objects.

For the biggest aperture the correction for the systematic fluorescence radiation changes the apparent mass attenuation coefficient by up to 0.0151% for the thinnest 10 μm foil and up to 0.153% and 15.5% for the 25 μm and 50 μm foils respectively; whilst for the smallest apertures these values reduce to 0.009%, 0.011% and 1.47% for the respective samples. These corrections combine to give corrections to the final attenuation across all apertures of 0.0123%, 0.101% and 14.2%. for the 10 μm 25 μm and 50 μm samples respectively.

Fig. 7 represents the discrepancy of the mass attenuation coefficients before and after correcting the effect of scattering and fluorescence radiation for the 50 μm thick sample foil in the region just above the edge where the impact is largest. The standard error on our mass attenuation coefficient before correction for fluorescence is about

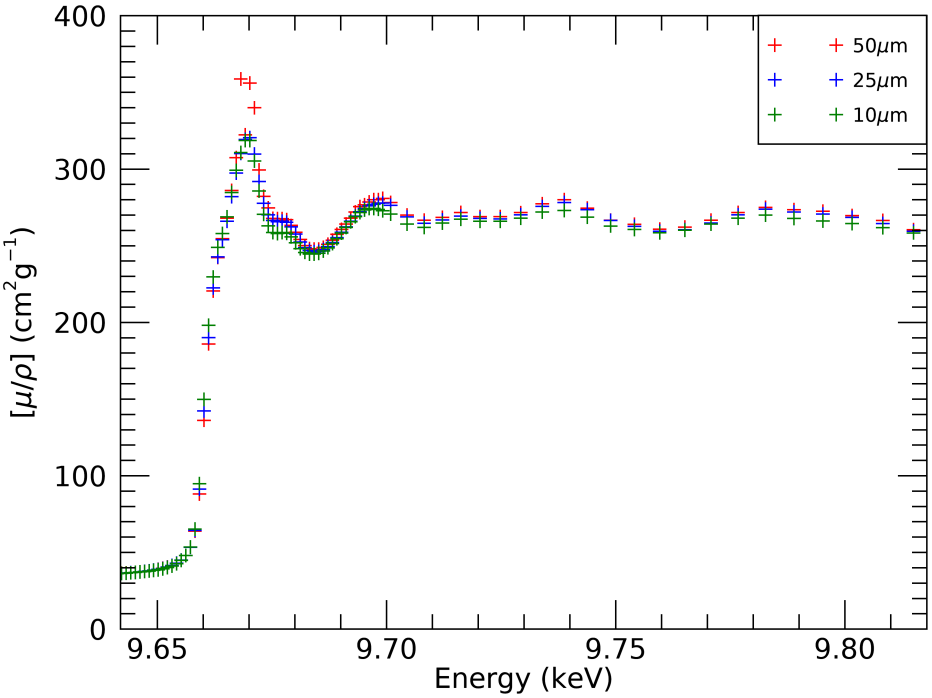

Figure 8. Mass attenuation coefficients of zinc materials from 10 μm, 25 μm and 50 μm thick sample foils in the edge region after correcting for the effect of fluorescence radiation.

0.042% or less. The application of the scattering correction improves this uncertainty, decreasing it by up to 50.5%; so that the total uncertainty of the mass attenuation coefficient after the scattering correction is reduced to about 0.028% or less. If the experiment only used a single thick sample the correction would be enormous and unknown. By measuring with several aperture combinations and with several thicknesses including blank measurements, the signatures are readily corrected for. We note that any Rayleigh (but not Laue-Bragg) scattering could be corrected for in the same manner.

The effect of scattering and fluorescence radiation is more prominent for thick sample foils. Herein, this effect is profound for 50 μm thick sample foils, particularly just after the edge energy (Fig. 8). After correcting for the effect of fluorescence radiation, some individual intensity points for the 50 μm sample immediately above the edge for the downstream detector become negative, so the log fails, for certain measurements, since the counts are very close to zero and the fluorescence is large. This yields large uncertainty at these energies for the 50 μm sample due to uncertainties in our dark current and fluorescent scattering model. Even slight variations have a large impact on the attenuation. At these energies, resulting uncertainties coming from 1. an error estimate of 8.66% in the fluorescent scattering signature and 2. ± 0.5 counts in the dark current range up to 22.02% and 21.7% respectively. Fig. 9 represents the contributions

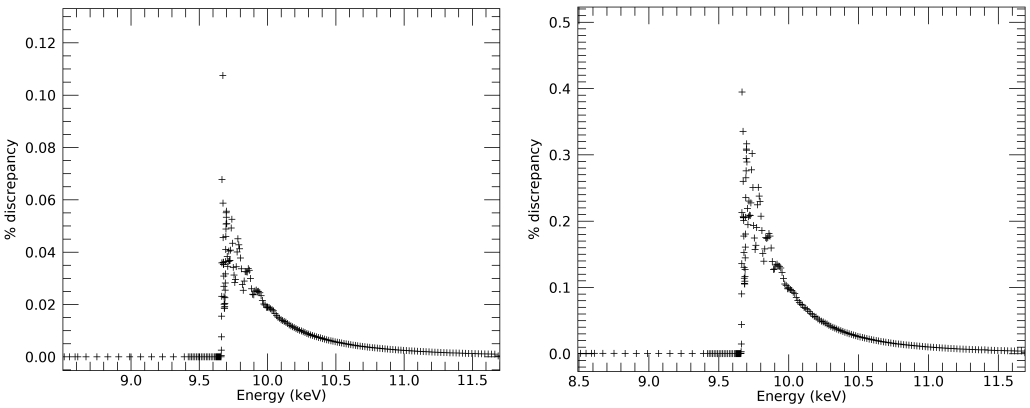

Figure 9. Percentage error introduced to the mass attenuation coefficient of the 50 μm sample due to uncertainty in both the modelled fluorescence signature (left) and dark current (right). A couple of energies at the white line have additional uncertainty up to 22.02% for the fluorescence scattering correction and 21.7% for dark current uncertainty from noise for the 50 μm sample, not seen for the 25 μm or 10 μm samples.

to uncertainty from these two components away from the white line. Accordingly, the weighted mean of results is dominated by measurements with 10 μm and 25 μm sample foils. The net result has uncertainties below 0.026% except for about 3 energies of the white line where the final uncertainty reaches 0.036%.

7. Conclusion

We demonstrated a method for investigating the absolute effect of fluorescence radiation on synchrotron X-ray measurements. The technique used X-ray attenuation measurements of zinc coming through different sized aperture combinations to explore the different amount of fluorescence radiation resulting in the synchrotron beam at energies between 8.5 keV and 11.59 keV. The differences of the mass attenuation coefficients measured with the different apertures and the smallest aperture combination were explored for different thick sample foils. The smallest aperture combination is the most stable so long as the beam is not thereby truncated, due to the minimum scattering contribution to the main beam. However, background fluorescence or other scattering from beamline optics can make this analysis more complex. Our technique introduces the background fluorescence contribution as observed, fitting well with the experimental data.

The effect of fluorescence radiation is an important key systematic error as the secondary photons entering the ion chambers misinterpret the true value of intensity counts and therefore of attenuation coefficients. Since this is thickness-dependent, it will incorrectly scale normalisation of fluorescence measurement by reference foils, or normalisation of transmission measurements by reference foils.

The effect of fluorescence can be quite large just above the absorption edge. The correction was implemented over the entire experimental energy range and resulted a

sudden increase in the change of the mass attenuation coefficients along the white line and negligible changes below the edge. The correction of the effect of fluorescence reduced standard errors by 0.0094% and hence the total standard error of the mass attenuation coefficients towards 0.028% or less. The impact of ignoring the scattering effect is clearly observed for zinc mass attenuation coefficients [24, 25]. The methodology used in the current work can be easily applied to many experiments due its accuracy and simplicity.

8. Acknowledgments

We sincerely acknowledge and are very grateful for the long and faithful collaboration with Zwi Barnea who has driven the development of XERT to investigate key systematics. Part of this research was undertaken on the XAS beamline at the Australian Synchrotron, part of ANSTO. We thank ANSTO and the Australian Synchrotron for their efforts and dedication to build up part of this methodology. We thank all of the synchrotron team including Peter Kappen, Bernt Johannessen, Jeremy Wykes, Chris Glover and Susan Cumberland for their support and dedication during the data collection. We thank Dr Chanh Tran, Martin Schalken, Alexis Illig, Daniel Sier, and Martin de Jonge for their contributions here and in earlier experiments.

9. Data Availability Statement

Data is available from the authors and also via [24, 25].

10. References

[1] W. Rontgen, "On a new kind of ray," *Nature*, vol. 53, pp. 274–276, 1896.

[2] M. D. de Jonge, C. Q. Tran, C. T. Chantler, Z. Barnea, B. B. Dhal, D. Paterson, E. P. Kanter, S. H. Southworth, L. Young, M. A. Beno, J. A. Linton, and G. Jennings, "Measurement of the x-ray mass attenuation coefficient and determination of the imaginary component of the atomic form factor of tin over the energy range of 29-60 keV," *Physical Review A*, vol. 75, no. 3, pp. 1–16, 2007.

[3] C. T. Chantler, C. Q. Tran, and Z. Barnea, "X-ray absorption fine structure for single crystals," *Journal of Applied Crystallography*, vol. 43, no. 1, pp. 64–69, 2010.

[4] V. A. Streltsov, R. S. Ekanayake, S. C. Drew, C. T. Chantler, and S. P. Best, "Structural Insight into Redox Dynamics of Copper Bound N-Truncated Amyloid-β Peptides from in Situ X-ray Absorption Spectroscopy," *Inorganic Chemistry*, vol. 57, no. 18, pp. 11422–11435, 2018.

[5] A. Di Cicco, "X-ray Absorption Spectroscopy investigations of disordered matter," *Radiation Physics and Chemistry*, pp. 108077 –1 –8, 2020.

[6] A. Kuzmin, J. Timoshenko, A. Kalinko, I. Jonane, and A. Anspoks, "Treatment of disorder effects in X-ray absorption spectra beyond the conventional approach," *Radiation Physics and Chemistry*, pp. 108112 –1 –8, 2020.

[7] A. Dehelean, S. Rada, and J. Zhang, "Determination of the lead environment in samarium - lead oxide-borate glasses and vitroceramics using XANES and EXAFS studies," *Radiation Physics and Chemistry*, pp. 108927 –1 –9, 2020.

[8] D. C. Creagh and J. H. Hubbell, "Problems associated with the measurement of Xray attenuation coefficients. I. Silicon. Report of the International Union of Crystallography Xray Attenuation Project," *Acta Crystallographica Section A*, vol. 43, no. 1, pp. 102–112, 1987.

[9] D. C. Creagh and J. H. Hubbell, "Problems associated with the measurement of Xray attenuation coefficients. II. Carbon. Report on the International Union of Crystallography Xray Attenuation Project," *Acta Crystallographica Section A*, vol. 46, no. 5, pp. 402–408, 1990.

[10] H. J. Krappe and H. H. Rossner, "Error analysis of EXAFS measurements," *Journal of Synchrotron Radiation*, vol. 6, no. 3, pp. 302–303, 1999.

[11] S. H. Southworth, L. Young, E. P. Kanter, and T. LeBrun, *X-Ray Scattering and Fluorescence from Atoms and Molecules*. National Institute of Standards and Technology, Gaithersburg, MD, USA, 1998.

[12] T. G. Gerward L., "X-ray Attenuation in Silicon and Germanium in the Energy Range 25 to 50 keV," *Z. Naturforsch.*, vol. 32 a, pp. 588–593, 1977.

[13] C. Q. Tran, M. D. de Jonge, Z. Barnea, and C. T. Chantler, "Absolute determination of the effect of scattering and fluorescence on x-ray attenuation measurements," *Journal of Physics B*, vol. 37, no. 04, pp. 3163–3176, 2004.

[14] J. H. Hubbell, "Compilation of Photon Cross-Sections: Some Historical Remarks and Current Status," *X-Ray Spectrometry*, vol. 28, no. 4, pp. 215–223, 1999.

[15] C. T. Chantler, "Detailed tabulation of atomic form factors, photoelectric absorption and scattering cross section, and mass attenuation coefficients in the vicinity of absorption edges in the soft X-ray (Z = 30-36, Z = 60-89, E = 0.1-10 keV)–addressing convergence issue," *Journal of Physical and Chemical Reference Data*, vol. 29, no. 4, pp. 597–1056, 2000.

[16] C. T. Chantler, C. Q. Tran, and Z. Barnea, "Measurement of the X-ray mass attenuation coefficient of copper using 8 . 85 20 keV synchrotron radiation," *Physical Review A*, vol. 64, pp. 062506(1–15), 2001.

[17] L. G. Parratt, J. O. Porteus, H. W. Schnopper, and T. Watanabe, "X-ray absorption coefficients and geometrical collimation of the beam," *Review of Scientific Instruments*, vol. 30, no. 5, pp. 344–347, 1959.

[18] D. C. Creagh, "On the measurement of mass absorption coefficients using a modified X-ray fluorescence spectrometer," *Journal of Physics E: Scientific Instruments*, vol. 9, no. 2, pp. 88–90, 1976.

[19] E. A. Stern and S. M. Heald, "X-ray filter assembly for fluorescence measurements of x-ray absorption fine structure absorption fine structure," *Review of Scientific Instruments*, vol. 1579, pp. 1579–1582, 2008.

[20] C. T. Chantler, C. Q. Tran, D. Paterson, D. Cookson, and Z. Barnea, "X-ray extended-range technique for precision measurement of the x-ray mass attenuation coefficient and im (f) for copper using synchrotron radiation," *Physics Letters A*, vol. 286, no. 5, pp. 338–346, 2001.

[21] E. A. Stern, "Detectors for laboratory EXAFS facilities," *AIP Conference Proceedings*, vol. 39, pp. 39–50, 2008.

[22] M. D. de Jonge, C. Q. Tran, C. T. Chantler, and Z. Barnea, "Improved techniques for measuring x-ray mass attenuation coefficients," *Optical Engineering*, vol. 45, no. 4, pp. 046501 1–8, 2006.

[23] J. L. Glover, C. T. Chantler, Z. Barnea, N. A. Rae, and C. Q. Tran, "Measurement of the x-ray mass-attenuation coefficients of gold, derived quantities between 14 keV and 21 keV and determination of the bond lengths of gold," *Journal of Physics B*, vol. 43, no. 8, pp. 085001(1–15), 2010.

[24] R. S. K. Ekanayake, C. T. Chantler, M. J. Schalken, A. J. Illig, D. Sier, M. D. de Jonge, B. Johannesen, P. Kappen, and C. Q. Tran, "High-accuracy mass attenuation coefficients and X-ray absorption spectroscopy of zinc the first X-ray Extended Range Technique-like experiment in Australia," *Journal of Synchrotron Radiation*, vol. 28, 2021.

[25] R. S. K. Ekanayake, C. T. Chantler, M. J. Schalken, A. J. Illig, D. Sier, M. D. de Jonge, B. Johannesen, P. Kappen, and C. Q. Tran, "High-accuracy measurement of mass attenuation

coefficients and the imaginary component of the atomic form factor of zinc from 8.51 keV to 11.59 keV, and X-ray absorption fine structure with investigation of zinc theory and nanostructure," *Journal of Synchrotron Radiation*, vol. 28, 2021.

[26] J. H. Hubbell, "Review of photon interaction cross section data in the medical and biological context," *Physics in Medicine and Biology*, vol. 44, no. 1, pp. R1–22, 1999.

[27] J. H. Hubbell, H. A. Gimm, and I. Overbo, "Pair, Triplet, and Total Atomic Cross Sections (and Mass Attenuation Coefficients) for 1 MeV - 100 GeV Photons in Elements Z=1 to 100," *Journal of Physical and Chemical Reference Data*, vol. 9, no. 4, pp. 1023–1148, 1980.

[28] M. J. Berger and J. H. Hubbell, "XCOM : Photon Cross Sections on A National Bureau of Standards NBSIR-87-3597," tech. rep., National Bureau of Standards, Washington, DC (USA). Center for Radiation, 1987.

[29] R. W. Fink, R. C. Jopson, H. Mark, and C. D. Swift, "Atomic fluorescence yields," *Reviews of Modern Physics*, vol. 38, no. 3, pp. 513–540, 1966.

[30] J. A. Bearden, "X-ray wavelengths," *Reviews of Modern Physics*, vol. 39, no. 1, pp. 78–124, 1967.

[31] C. T. Chantler, L. F. Smale, and L. T. Hudson, "X-ray energies," in *International Tables for Crystallography, Vol. C* (T. R. Welberry, ed.), ch. 4.2.2, Dordrecht: Kluwer Academic Publishers, 2020.

[32] M. O. Krause, "Atomic radiative and radiationless yields for K and L shells," *Journal of Physical and Chemical Reference Data*, vol. 8, no. 2, pp. 307–327, 1979.

[33] J. Jaklevic, J. A. Kirby, M. P. Klein, A. S. Robertson, B. Laboratories, and M. Hill, "Solid State Communications, Vol. 23,," *Solid State Communications*, vol. 23, no. 3, pp. 679–682, 1977.

[34] H. Hayashi, R. Takeda, Y. Udagawa, T. Nakamura, H. Miyagawa, H. Shoji, S. Nanao, and N. Kawamura, "Lifetime-broadening-suppressed/free xanes spectroscopy by high-resolution resonant inelastic x-ray scattering," *Physical Review B*, vol. 68, no. 4, p. 045122, 2003.

[35] F. De Groot and A. Kotani, *Core level spectroscopy of solids*. CRC press, 2008.

[36] L. Troger, D. Arvanitis, and K. Baberschke, "Full correction of the absorption in soft-fluorescence extended x-ray absorption fine structuer," *Physical Review B*, vol. 46, pp. 3283–3289, 1992.

[37] C. T. Chantler, N. A. Rae, M. T. Islam, S. P. Best, J. Yeo, L. F. Smale, J. Hester, N. Mohammadi, and F. Wang, "Stereochemical analysis of ferrocene and the uncertainty of fluorescence XAFS data," *Journal of Synchrotron Radiation*, vol. 19, no. 2, pp. 145–158, 2012.

[38] R. M. Trevorah, C. T. Chantler, and M. J. Schalken, "Solving self-absorption in fluorescence," *IUCrJ*, vol. 6, no. 2025-2525, pp. 586–602, 2019.

[39] S. Kraft, J. Stümpel, P. Becker, and U. Kuetgens, "High resolution x-ray absorption spectroscopy with absolute energy Calibration for the determination of absorption edge energies," *Rev. Sci. Instrum.*, vol. 67, no. 3, pp. 681–687, 1996.

[40] W. Bambynek, B. Crasemann, R. W. Fink, H. U. Freund, H. Mark, C. D. Swift, R. E. Price, and P. V. Rao, "X-ray fluorescence yields, auger, and coster-kronig transition probabilities," *Reviews of Modern Physics*, vol. 44, no. 4, pp. 716–813, 1972.

[41] C. T. Chantler, "Theoretical Form Factor, Attenuation, and Scattering Tabulation for Z=192 from E=110 eV to E=0.41.0 MeV," *Journal of Physical and Chemical Reference Data*, vol. 24, no. 1, pp. 71–643, 1995.

[42] C. Q. Tran, C. T. Chantler, Z. Barnea, M. D. de Jonge, B. B. Dhal, C. T. Chung, D. Paterson, and J. Wang, "Measurement of the x-ray mass attenuation coefficient of silver using the x-ray-extended range technique," *Journal of Physics B*, vol. 38, no. 1, pp. 89–107, 2005.